Energy 307 (2024) 132617

Contents lists available at ScienceDirect

Energy

journal homepage: www.elsevier.com/locate/energy

A novel microgroove-based absorber for sorption heat transformation systems: Analytical modeling and experimental investigation

Mahyar Ashouri, Callum Chhokar, Majid Bahrami *

Pacific Institute for Climate Solutions and Laboratory for Alternative Energy Conversion (LAEC), School of Mechatronic Systems Engineering, Simon Fraser University, Surrey, BC, V3T 0A3, Canada

ARTICLE INFO

Keywords:
Sorption heat transformers
Microgroove
Superhydrophilic
Heat and mass transfer
Analytical model
Thin film

ABSTRACT

This study proposes a novel sorber bed design, a stationary thin film microgroove-based absorber, that can address the low specific power and oversized sorber bed issues in existing oscillatory solid sorption heat transformation systems. An analytical heat and mass transfer model is developed for the proposed stationary thin film microgroove-based absorber. A highly-wettable microgrooved aluminum substrate is fabricated by the deposition of a hybrid Al_2O_3/TiO_2 layer, and experimental water uptake measurements are obtained using a custom-built gravimetric large pressure jump setup to validate the analytical model. The model examines how key design parameters affect specific cooling power, cooling power density, and energy storage density. Findings indicate that cycle time and groove depth significantly impact system performance. Also, it is found that there is an optimum groove depth, or film thickness, to achieve maximum power. Trapezoidal grooves achieve higher specific cooling power and cooling power density, while rectangular grooves yield a higher maximum energy storage density. It is experimentally shown that a specific cooling power enhancement of up to 600 % can be obtained compared to the experimental data available for oscillatory sorber beds. Also, the absorption rate of the present sorber bed is up to three times higher than that of falling film absorbers.

Nomenclature

c	Concentration of absorbate, [kg.kg^{-1}]
$\mathbf{c_p}$	Isobaric specific heat, [J·kg^{-1}K^{-1}]
D_s	Mass diffusivity, [m^2·s^{-1}]
D	Groove depth [m]
Fo	Fourier number, non-dimensional time
g	Gravity, [m·s^{-2}]
$h_{sor/des}$	sorption heat, [J. kg^{-1}]
h_{fg}	Enthalpy of evaporation [J. kg^{-1}]
p	Pressure, [Pa]
Le	Lewis number, [*Le*= α.D^{-1}]
$\dot{q}$	Heat flux, [W·m^{-2}]
Q	Heat [J]
R_m	Meniscus radius, [m]
T	Temperature, [K]
t	Time, [s]
t_w	Wall thickness [μm]
W	Groove width [μm]
y	Local normal position, [m]
Greek symbols	
α	Thermal diffusivity, [m^2·s^{-1}]

(*continued on next column*)

(*continued*)

γ	Dimensionless concentration
Υ	Dimensionless concentration in the Laplace space
η	Dimensionless normal position
Λ	Normalized heat of absorption
ω	Uptake, [g water/g sorbent]
τ	Cycle time, sorption plus desorption
θ	Dimensionless temperature
Θ	Dimensionless temperature in the Laplace space
δ	Film thickness, [μm]
ρ	Density, kg·m^{-3}
Subscripts	
ave	Average
eva	Evaporator
eq	Equilibrium
eqv	Equivalent
inf	Interface
o	Entrance region
s	Solution
HEX	Heat exchanger
v	Vapor
w	Wall

* Corresponding author.
E-mail address: mbahrami@sfu.ca (M. Bahrami).

https://doi.org/10.1016/j.energy.2024.132617
Received 8 April 2024; Received in revised form 25 July 2024; Accepted 26 July 2024
Available online 2 August 2024

1. Introduction

Global industrial processes generate significant waste heat, released through mediums such as solid waste, waste gas, and waste water. Recovering industrial waste heat offers a considerable opportunity for substantial energy savings and emission reductions. Among the various types of waste heat, low-grade waste heat constitutes approximately 60 % and is the most challenging to recover [1,2]. Consequently, there is extensive research focused on heat-driven sorption systems [3,4].

Sorption heat transformation systems [5–9] can effectively perform heat transformation and upgrade low-grade waste heat while minimizing electric power usage. In contrast to heating, which can be achieved through the direct use of waste heat, cooling can be more challenging. The most industrialized option is vapor compression refrigeration systems, which operate on global-warming potential refrigerants [10]. The specific cooling power per total system mass for available solid sorption cooling systems ranges from 15.9 to 45.4 W/kg, whereas for vapor compression refrigeration, it ranges from 113 to 160 W/kg [11]. Thus, current sorption technologies necessitate significant improvements in specific power, maintenance, and, crucially, cost-effectiveness. The design of the sorber bed plays a critical role as it directly impacts the sorption rate, which affects the performance and dimensions of the sorption systems.

Sorption heat transformation systems can also provide long-term heat storage with minimal loss since the primary storage mechanism is a thermochemical reaction. They facilitate the conversion of excess power into heat/cold (along with storage), which is crucial for integrating renewable energy. While sorption storage systems operate on the same cycle, the components need to be optimized, necessitating different solid sorbent/liquid film thicknesses, and thermal characteristics when compared to heat transformation and upgrading purposes.

These sorption systems are categorized into continuous cycle and oscillatory cycle systems. Continuous cycle absorption systems consist of four components: absorber, desorber, evaporator, and condenser. They provide continuous heating/cooling power through a continuous flow of solution between the absorber and desorber. Oscillatory sorption heat transformation systems are designed using solid sorbents, or adsorbents, so far. Sorbent materials include mesoporous silicates, classical zeolites, (silico)aluminophosphates, porous coordination polymers (PCPs), porous carbons, composite sorbents, and salt hydrates [12]. Mesoporous silicates like silica gel are effective for moisture removal in various industries due to their hydrophilic surfaces [13]. Classical zeolites, known for their tailored water uptake abilities based on Si/Al ratios, excel in gas drying applications but require high desorption temperatures [14]. Aluminophosphates and SAPOs offer structural stability and are promising for low-grade heat applications [15]. Porous coordination polymers, such as MOFs, provide tunable pore sizes and high surface areas, suitable for diverse sorption tasks despite low temperature efficiency [16]. Activated carbons are also used in sorption processes, especially with non-aqueous substances like methanol [17]. A composite sorbent is created by impregnating a porous host matrix (e.g., silica gel) with a hygroscopic salt (e.g., $CaCl_2$) for high uptake capacities [18]. Salt hydrates, with high energy densities and low desorption temperatures, are promising for thermal energy storage despite challenges like deliquescence in humid conditions [19].

Oscillatory sorption heat transformation systems have three components: sorber bed, evaporator, and condenser. During sorption, the evaporator produces water vapor that is absorbed by the sorber bed, generating useful heat. During desorption, input heat causes water vapor to be desorbed in the sorber bed and to condense in the condenser. As a result, the sorber bed's temperature oscillates between sorption and desorption temperatures. Multiple sorber beds enable continuous output. The sorber bed design is crucial for system performance, and various studies have investigated different types of sorber beds. Table 1 compares these sorber bed types used in sorption heat transformation systems.

Table 1
Comparison of different sorber beds used in sorption heat transformation systems [6,20–31].

System type	Type of sorber bed	Advantages	Disadvantages
Continuous cycle	Falling films	✓ Easy to manufacture ✓ Cost-effective ✓ High heat transfer surface	× Crystallization × Low absorption rate and performance caused by flow separation, low adjustability of film thickness, and low surface wetting ratio × Bulky and oversized design × Maintenance and sealing issues
	Bubble flows	✓ Easy to manufacture ✓ Cost-effective ✓ High mass transfer surface	× Low heat transfer surface × Toxic and flammable working pairs × Miscellaneous parts, such as rectifier
	Membrane-based absorbers	✓ High sorption rate, and thus, high performance ✓ Compact	× Crystallization × High-pressure drop within solution channels × Membrane failure × Maintenance and sealing issues × Expensive to manufacture
Oscillatory cycle	Solid sorbent	✓ Crystallization is not an issue ✓ Cost-effective ✓ No moving parts	× Low performance due to low thermal conductivity (0.1–0.2 W/m.K), limited salt ratio (20–30 %), and high thermal contact resistance between sorbent and heat exchanger × Salt leakage × Bulky and oversized design × Maintenance and sealing issues
	Stationary thin film absorber (present study)	✓ High sorption rate, and thus, high performance ✓ Crystallization is not a critical issue compared to falling film absorbers ✓ Compact ✓ No moving parts	× Expensive to manufacture due to groove fabrication and surface modification × Maintenance and sealing issues

As mentioned in Table 1, solid sorbents are inhibited by several factors: i) the host matrix's low thermal conductivity (~0.1–0.2 W/m·K) limits heat transfer and sorption rates, despite attempts to improve it with additives like natural graphite flakes, which in turn increase inactive mass, ii) high thermal contact resistance between the solid sorbent and heat exchanger walls further reduces heat transfer efficiency, and iii) limitations on salt percentage (20–30 %) to prevent runoff result in low sorption uptake since salt is the primary sorbent.

In this study, we propose the first absorption-based and porous media-free sorber bed for oscillatory sorption heat transformation systems, called a stationary thin film absorber. This sorber bed consists of a stationary film solution, such as aqueous LiBr, confined within surface microstructures. In this study, the microstructures are grooves; thus, the microgroove-based absorber is proposed. Unlike solid sorber beds, the present stationary film absorber is unaffected by limitations like low

thermal conductivity (about 0.5 W/m.K), high thermal contact resistance (ideal heat transfer between the film and substrate), or low salt percentage (about 70 %). Although the present sorber bed addresses the heat transfer limitations of solid sorber beds, using a liquid film may introduce mass transfer limitations (water vapor diffusion), which can be mitigated by employing thin films to reduce the diffusion path length.

An analytical heat and mass transfer model is developed for the proposed stationary thin film microgroove-based absorber. A highly-wettable microgrooved aluminum substrate is fabricated by the deposition of a hybrid Al_2O_3/TiO_2 layer, and experimental water uptake measurements are obtained using a custom-built gravimetric large pressure jump setup to validate the analytical model. The model examines how key design parameters affect specific cooling power, cooling power density, and energy storage density. Also, the system's performance in terms of specific cooling power (SCP) and coefficient of performance (COP) is compared to the experimental studies in the literature.

2. Model development

This section presents the microgroove-based absorber as an embodiment of the proposed stationary thin film absorber (Fig. 1a). During the absorption cycle (Fig. 1b), water vapor is introduced into the absorber chamber and absorbed by the solution. The exothermic absorption process increases the solution temperature, reducing the absorption rate. The solution is cooled using a heat transfer fluid to maintain absorption. The desorption cycle (Fig. 1c) follows the reverse mechanism, where the solution is heated by adjusting the temperature of the heat transfer fluid, causing water vapor desorption.

The present model assumptions, also documented in Ref. [25], are as follows.

- 1D heat and mass transfer.
- An equivalent thermal conductivity captures the heat conduction through the microgrooves wall [32].
- An averaged film thickness is used.
- A linear equilibrium exists between the solution temperature and concentration at the solution-vapor interface at a constant vapor pressure (Eq. (10)).
- Isothermal heat exchanger wall.
- Constant thermophysical properties.
- Non-volatile absorbent.
- Negligible heat transfer from the film to the gas phase (vapor) – the system operates under vacuum conditions.

Assuming " y " for diffusion direction, the governing equations for energy and species conservation can be derived as follows:

$$\frac{\partial T}{\partial t} = \alpha_s \frac{\partial^2 T}{\partial y^2} \tag{1}$$

$$\frac{\partial c}{\partial t} = D_s \frac{\partial^2 c}{\partial y^2} \tag{2}$$

Where , T, α_s, and D_s are the solution's temperature, thermal diffusivity, and mass diffusivity, respectively. It should be noted that "c" is the water (absorbate) concentration (kg water/kg solution), not the salt concentration (kg LiBr/kg solution). Using the equilibrium temperature and concentration, Eqs. (1) and (2) can be non-dimensionalized. The equilibrium temperature $''T_{eq}''$ is defined as the temperature at the inlet concentration $''c_o''$ and the water vapor pressure $''p_v''$; similarly, the equilibrium concentration $''c_{eq}''$ is defined as the concentration at the inlet temperature $''T_o''$ and the water vapor pressure $''p_v''$ [33]. Equilibrium temperature and concentration can be calculated via a phase equilibrium equation, see Appendix A. The energy and species conservation equations can be written in non-dimensional form as follows:

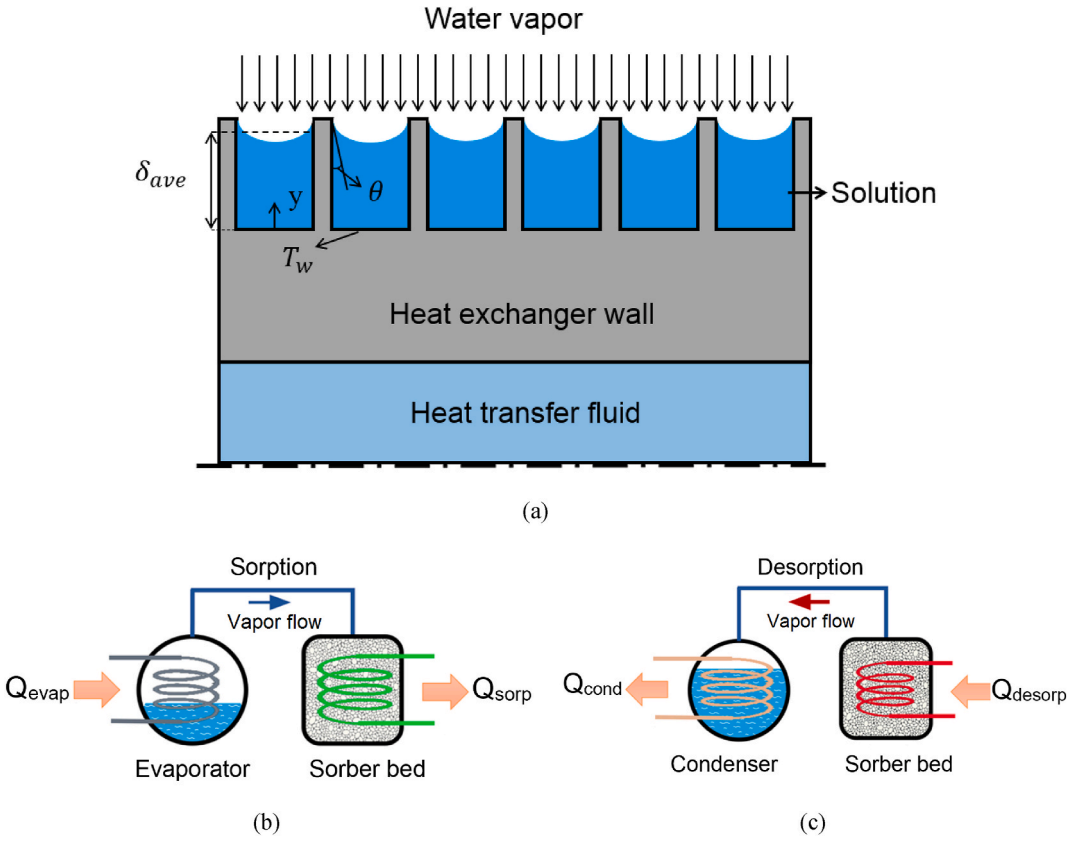

Fig. 1. Schematic of (a) a microgroove-based absorber, an embodiment of the stationary thin film absorber concept, (b) sorption cycle, and (c) desorption cycle.

$$\frac{\partial\theta}{\partial Fo}=\frac{\partial^2\theta}{\partial\eta^2} \tag{3}$$

$$Le\frac{\partial\gamma}{\partial Fo}=\frac{\partial^2\gamma}{\partial\eta^2} \tag{4}$$

$$\Theta(\xi,\eta)=\frac{T(Fo,\eta)-T_o}{T_{eq}(c_o,p)-T_o}, \tag{5}$$

$$\gamma(\xi,\eta)=\frac{c(Fo,\eta)-c_o}{c_{eq}(T_o,p)-c_o} \tag{6}$$

$$Fo=\frac{\alpha_s}{\delta_{ave}^2}t \quad \& \quad \eta=\frac{y}{\delta_{ave}} \tag{7}$$

where, θ, Fo, γ, and η represent non-dimensional temperature, Fourier number or non-dimensional time, non-dimensional concentration, and non-dimensional $''y''$, respectively. The initial and boundary conditions of the isothermal, impermeable wall are as follows:

$$Fo=0\Longrightarrow\begin{cases}\Theta(0,\eta)=\dfrac{T_o-T_o}{T_{eq}(c_o,p)-T_o}=0\\ \gamma(0,\eta)=\dfrac{c_o-c_0}{c_{eq}(T_o,p)-c_o}=0\end{cases} \tag{8}$$

$$\eta=0\Longrightarrow\begin{cases}\Theta(Fo,0)=\dfrac{T_w-T_o}{T_{eq}(c_o,p)-T_o}=\Theta_w\\ \left.\dfrac{\partial\gamma}{\partial\eta}\right|_{\eta=0}=0\end{cases} \tag{9}$$

$$\eta=1\Longrightarrow\begin{cases}\Theta(Fo,1)+\gamma(Fo,1)=1\\ \left.\dfrac{\partial\Theta}{\partial\eta}\right|_{inf}=\dfrac{\Lambda}{Le}\left.\dfrac{\partial\gamma}{\partial\eta}\right|_{inf}\end{cases} \tag{10}$$

$$\Lambda=\frac{h_{abs}(c_{eq}-c_o)}{c_{p,s}(T_{eq}-T_o)}, Le=\frac{\alpha_s}{D_s} \tag{11}$$

The detailed solution procedure, using Laplace transform and similarity solution methods, is provided in Appendix B. The analytical solutions obtained from the temperature and concentration profiles (see Appendix B) are used to determine the uptake and heat generation values for stationary solution film absorbers with microgrooves. The corresponding results are summarized in Table 2.

This study employs an equivalent thermal conductivity and average film thickness following the assumptions. The equations for determining the porosity, equivalent thermal conductivity, and average film thickness for rectangular and trapezoidal grooves are presented in Table 3. Further details can be found in Appendix C.

3. Experimental setup

3.1. Absorber fabrication

A 6 cm by 6 cm aluminum substrate with a thickness of 1.5 mm was

Table 3
Porosity, equivalent thermal conductivity, and average film thickness equations for rectangular and trapezoidal grooves.

Groove type	Equation	Equation No.
	$k_{eqv}=k_s\frac{[(k_s+k_w)-(1-\phi)(k_s-k_w)]}{[(k_s+k_w)+(1-\phi)(k_s-k_w)]}$ [32]	(16)
Rectangular groove 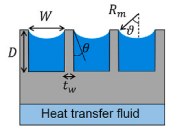	$\delta_{ave}=D+0.5\sqrt{R_m^2-\frac{W^2}{4}}-\frac{\vartheta R_m^2}{W}$ [m]	(17)
	$\phi=\frac{D+0.5\sqrt{R_m^2-\frac{W^2}{4}}-\frac{\vartheta R_m^2}{W}}{D(t+W)}$	(18)
Trapezoidal groove 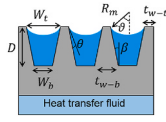	$\delta_{ave}=\frac{W_t+W_b}{2}\frac{D}{W_t}+0.5\sqrt{R_m^2-\frac{W_t^2}{4}}-\frac{\vartheta R_m^2}{W_t}$ [m]	(19)
	$\phi=\frac{\frac{W_t+W_b}{2}D+\frac{W_t}{2}\sqrt{R_m^2-\frac{W_t^2}{4}}-\vartheta R_m^2}{D(t_{w-t}+W_t)}$	(20)

Table 2
Closed-form relationships for calculating the uptake and heat generation in the microgroove-based absorber with a stationary solution thin film.

Parameter	Equation	
Uptake $\left[\frac{gr\ water}{gr\ sorbent}\right]$	$\omega(Fo)=\frac{m_{absorbed\ water\ @Fo}}{m_{dried\ sorbent}}=\frac{1}{1-[\overline{\gamma}(Fo)(c_{eq}-c_o)+c_o]}-\frac{1}{1-c_o}$	(12)
	$\overline{\gamma}(Fo)=\left[\left(1-\frac{\Theta_w\left(1+\frac{2\Psi}{Fo.\pi^2}\right)+\frac{8.\Omega.\Lambda}{Fo.\pi^2}}{1+\frac{2\Phi}{Fo.\pi^2}+\frac{8.\Omega.\Lambda}{Fo.\pi^2}}\right)\left(1-\sum_{k=0}^{\infty}\frac{8}{\pi^2(2k+1)^2}e^{-\frac{(2k+1)^2\pi^2}{4Le}Fo}\right)\right]$	(13)
Heat generation $\left[\frac{W}{m^2}\right]$	$\dot{q}(Fo)=\frac{k_s(T_{eq}-T_o)}{\delta}\left[\overline{\Theta}_{inf}-\Theta_w+2\sum_{k=1}^{\infty}\left(\overline{\Theta}_{inf}+(-1)^{k+1}\Theta_w\right)e^{-k^2\pi^2Fo}\right]$	(14)
	$\overline{\Theta}_{inf}=\frac{\left(1+\frac{2\Psi}{Fo.\pi^2}\right)\Theta_w+\frac{8.\Omega.\Lambda}{Fo.\pi^2}\left(1-\frac{\Theta_w\left(1+\frac{2\Psi}{Fo.\pi^2}\right)+\frac{8.\Omega.\Lambda}{Fo.\pi^2}}{1+\frac{2\Phi}{Fo.\pi^2}+\frac{8.\Omega.\Lambda}{Fo.\pi^2}}\right)}{1+\frac{2\Phi}{Fo.\pi^2}}$	(15)
	$\Phi=\sum_{k=1}^{\infty}\frac{1}{k^2}\left(1-e^{-k^2\pi^2Fo}\right)\quad\Psi=\sum_{k=1}^{\infty}\frac{(-1)^k}{k^2}\left(1-e^{-k^2\pi^2Fo}\right)\quad\Omega=\sum_{k=0}^{\infty}\frac{1}{(2k+1)^2}\left(1-e^{-\frac{(2k+1)^2\pi^2}{4Le}Fo}\right)$	
	$\Theta(Fo,\eta)=\frac{T(Fo,\eta)-T_o}{T_{eq}(c_o,p_v)-T_o}\quad\gamma(Fo,\eta)=\frac{c(Fo,\eta)-c_o}{c_{eq}(T_o,p_v)-c_o}\quad\Lambda=\frac{h_{abs}c_o}{c_{p,s}T_o}\quad\eta=\frac{y}{\delta}\quad Fo=\frac{\alpha_s}{\delta^2}t\quad Le=\frac{\alpha_s}{D_s}$	

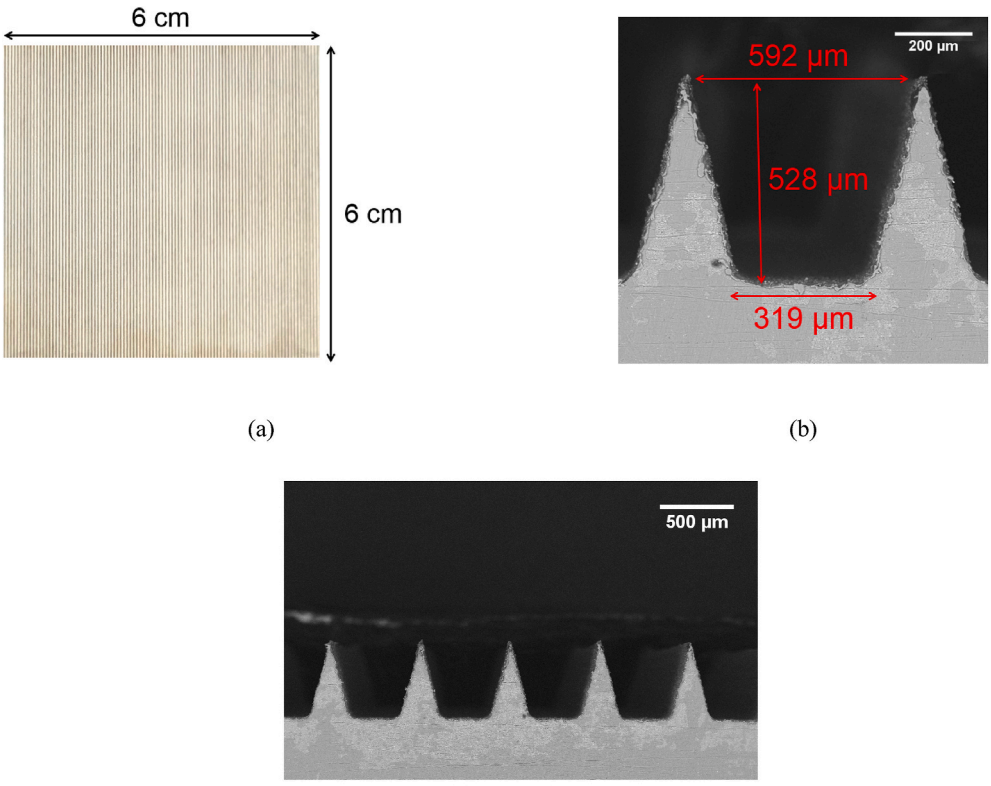

Fig. 2. (a) Microgrooved aluminum substrate and (b) and (c) SEM section view of the grooves.

fabricated using a wire electrical discharge machining to create microgrooves (Fig. 2). The grooves had trapezoidal shapes with dimensions of approximately 600 µm (top width), 320 µm (bottom width), and 530 µm (depth). The microgrooved aluminum substrate was coated with Al_2O_3/TiO_2 layers to enhance wettability and confine the solution within the microgrooves. Plasma-enhanced atomic layer deposition (Cambridge NanoTech Fiji F200) and magnetron-sputtering physical vapor deposition (Kurt J Lesker PVD75) techniques were utilized for the coating process. The wettability of the hybrid oxide coating was evaluated through contact angle measurements (sessile droplet method). A contact angle of approximately 21° was observed when a droplet of aqueous LiBr with a 60 % concentration was applied (see Appendix D for further details).

3.2. Gravimetric large pressure jump (GLPJ)

The sorption dynamics of the microgroove-based absorber were examined using a custom-built gravimetric large pressure jump (GLPJ) testbed (Fig. 3). The testbed consisted of a balance, vacuum chamber, evaporator, microchannel heat exchanger (cold plate), and two thermal baths. Refer to Ref. [29] for more comprehensive information regarding the testbed. The sorber bed was charged with 2.17 gr of the aqueous LiBr solution with a concentration of 65 %. The thermal bath was connected to the sorber bed during the experiments and maintained at 30 °C. Three evaporator temperatures of 5, 10, and 15 °C were used in this experiment.

Large pressure jump tests are performed by changing the relative

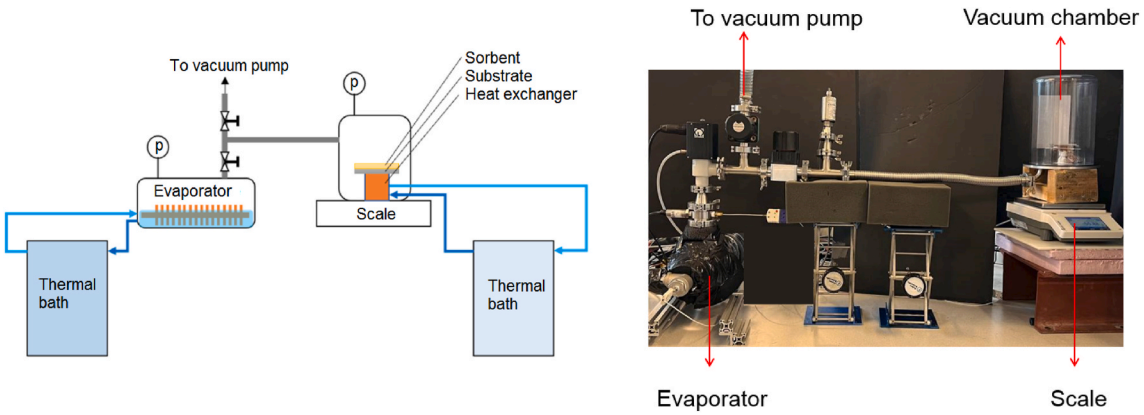

Fig. 3. (a) Schematic and (b) photograph of the gravimetric large pressure jump (GLPJ) testbed [29]. Thermal baths are not shown.

pressure, $\frac{p}{p_o}$, where "p" is the saturation pressure of the water vapor at the vapor temperature (which corresponds to the condenser temperature at the initial equilibrium and the evaporator temperature at the final equilibrium) and "p_o" is the saturation pressure of the water vapor at the sorber bed temperature. Therefore, the relative pressure, $\frac{p}{p_o}$, of the chamber was varied from a relative humidity of 0.06 ($\frac{p}{p_o} = \frac{p_{sat\ @\ 30^oC}}{p_{sat\ @\ 90^oC}}$) to 0.2 ($T_{eva}$= 5 °C, $\frac{p}{p_o} = \frac{p_{sat\ @\ 5^oC}}{p_{sat\ @\ 30^oC}}$), 0.29 ($T_{eva}$= 10 °C, $\frac{p}{p_o} = \frac{p_{sat\ @\ 10^oC}}{p_{sat\ @\ 30^oC}}$), and 0.4 ($T_{eva}$= 15 °C, $\frac{p}{p_o} = \frac{p_{sat\ @\ 15^oC}}{p_{sat\ @\ 30^oC}}$), Refer to Fig. 4 for the initial and final conditions of the isotherm.

3.3. Thermogravimetric sorption analysis

Water sorption isotherm for the aqueous LiBr used in this study was determined using an IGA-002 thermogravimetric sorption analyzer (TGA). Further information about the TGA can be found in Ref. [34]. A 30 °C isotherm was determined for relative humidities between 0 and 0.4 (Fig. 4). Also, the present isotherm is validated with the available experimental data in Ref. [35].

3.4. Performance parameters and uncertainty analysis

The performance parameters analyzed in this study include specific cooling power (SCP), cooling power density (CPD), energy storage density (ESD), Coefficient of Performance (COP), and mass ratio. SCP represents the rate of evaporative cooling per unit mass of dry sorbent material. CPD, on the other hand, quantifies the rate of evaporative cooling per unit volume of the sorber bed, indicating its compactness. ESD denotes the maximum amount of stored energy per unit volume of the sorber bed. COP shows the ratio of output power to the input power. Also, the mass ratio shows the ratio of the heat exchanger (metal) mass to the sorbent mass. The equations for these performance parameters are as follows:

$$SCP = \frac{Q_{eva}}{m_s\,\tau} = \frac{m_s \int \frac{d\omega}{dt} h_{fg} dt}{m_s\,\tau} = \frac{\Delta\omega\, h_{fg@T_{evap}}}{\tau} \left[\frac{kW}{kg}\right] \tag{21}$$

$$CPD = \frac{Q_{eva}}{V_{sys}\tau} = \frac{m_s \int \frac{d\omega}{dt} h_{fg} dt}{V_{sys}\tau} = \frac{m_s \Delta\omega\, h_{fg@T_{evap}}}{V_{sys}\tau} \left[\frac{kW}{m^3}\right] \tag{22}$$

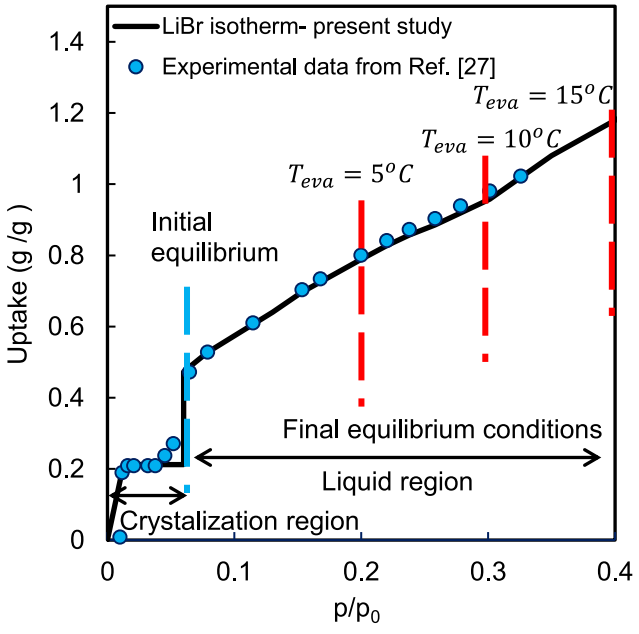

Fig. 4. 30 °C isotherm for aqueous LiBr.

$$ESD = \frac{Q_{eva}}{V_{sys}} = \frac{\Delta\omega\, m_s\, h_{fg}}{V_{sys}} \left[\frac{MJ}{m^3}\right] \tag{23}$$

$$COP = \frac{Q_{eva}}{Q_{input}} = \frac{m_s \int \frac{d\omega}{dt} h_{fg} dt}{\int \left[\left(m_{sorb}\left(c_{p,s} + \omega c_{p,w}\right) + m_{HEX} c_{p,HEX}\right)\frac{dT}{dt} - m_s \frac{d\omega}{dt} h_{des}\right] dt} \tag{24}$$

$$Mass\ ratio\ (MR) = \frac{m_{HEX}}{m_s} \tag{25}$$

where, Q_{eva} is the evaporative cooling energy, m_s is the sorbent mass, ω is the sorbate uptake ($g_{sorbate}\, g^{-1}_{dried\ sorbent}$), h_{fg} is the enthalpy of evaporation, τ is the cycle time (sorption + desorption), V_{sys} is the total volume of the system, Q_{input}[J] is the input heat, $c_{p,s}$ [J /kg.K] is the sorbent's specific heat, $c_{p,HTF}$ [J /kg.K] is the heat transfer fluid's specific heat, $c_{p,HEX}$ [J /kg.K] is the heat exchanger's wall specific heat, h_{des} is desorption heat, m_{HEX} is heat exchanger mass, and m_s is sorbent mass. The instrumental uncertainty associated with the measurements of SCP and ESD was determined using the method developed by Moffat [36]. The same approach was employed in a previous study conducted by Bahrehmand et al. [29] and is as follows:

$$\frac{\delta\omega}{\Delta\omega} = \frac{0.01\ gr}{m_s} = 0.3\% \tag{26}$$

$$\frac{\delta SCP}{SCP} = \frac{\delta\Delta\omega}{\Delta\omega} = \frac{\sqrt{2}\delta\omega}{\Delta\omega} = 0.5\% \tag{27}$$

$$\frac{\delta CPD}{CPD} = \frac{\delta\Delta\omega}{\Delta\omega} = \frac{\sqrt{2}\delta\omega}{\Delta\omega} = 0.5\% \tag{28}$$

$$\frac{\delta ESD}{ESD} = \sqrt{\left(\frac{\delta\Delta\omega}{\Delta\omega}\right)^2 + \left(\frac{\delta m_s}{m_s}\right)^2} \cong \frac{\sqrt{2}\delta\omega}{\Delta\omega} = 0.5\% \tag{29}$$

$$\frac{\delta COP}{COP} = \frac{2\delta\omega}{\Delta\omega} \approx 0.7\% \tag{30}$$

Five tests were conducted under consistent conditions, yielding a maximum standard deviation of 8 % for the uptake measurements. This relative standard deviation also applies to the SCP, CPD, ESD, and COP measurements due to their linear relationship with the uptake. The uncertainties for all four performance metrics (uptake, SCP, CPD, ESD, and COP) were determined by considering both instrumental and standard uncertainty. Uncertainties for all metrics were found to be below 9%.

4. Results and discussion

4.1. Model validation

The model is validated with experimental data from the gravimetric large pressure jump (GLPJ) tests. As mentioned, these tests were conducted with pressure jumps from a relative humidity of 0.064 ($\frac{p}{p_o} = \frac{p_{sat\ @\ 30^oC}}{p_{sat\ @\ 90^oC}}$) to 0.2 ($T_{eva}$= 5 °C, $\frac{p}{p_o} = \frac{p_{sat\ @\ 5^oC}}{p_{sat\ @\ 30^oC}}$), 0.29 ($T_{eva}$= 10 °C, $\frac{p}{p_o} = \frac{p_{sat\ @\ 10^oC}}{p_{sat\ @\ 30^oC}}$), and 0.4 ($T_{eva}$= 15 °C, $\frac{p}{p_o} = \frac{p_{sat\ @\ 15^oC}}{p_{sat\ @\ 30^oC}}$).

Fig. 5 shows the water uptakes of aqueous LiBr at three different evaporator temperatures (5, 10, and 15 °C). The average thermophysical properties of the LiBr-water solution used in the current model are presented in Table 4. The model demonstrates good agreement with the experimental data, with a mean relative difference of less than 8 %. Additionally, it can be observed that increasing the evaporator temperature leads to a higher maximum uptake capacity due to a more significant difference between initial and final equilibrium concentrations.

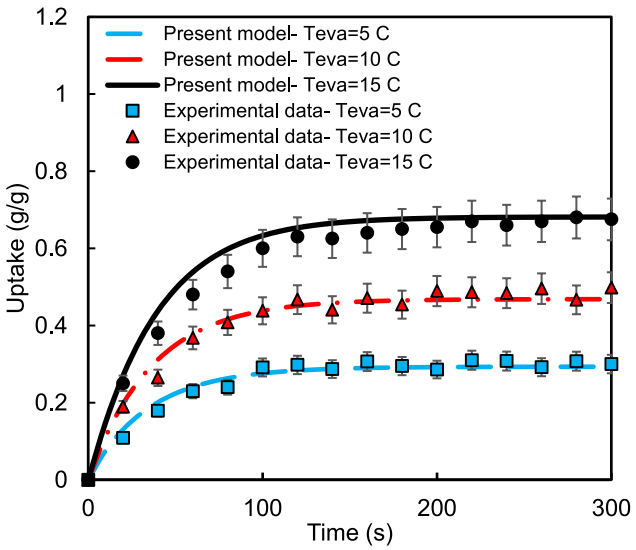

Fig. 5. Validation of the present model. Water uptake over time for different evaporator temperatures: 5, 10, and 15 °C.

Table 4
Thermal properties of aqueous LiBr [10,33,37].

Parameter	Value
Heat of absorption (kJ/kg)	2500
Mass transfer coefficient (m^2/s)	10^{-9}
Solution thermal conductivity (W/m.K)	0.44
Solution specific heat (J/kg.K)	2000
Solution density (kg/m^3)	1600

4.2. *Effects of key design parameters*

Using the present analytical model, this study investigates the influence of design parameters, such as groove geometry and cycle time, on specific cooling power, cooling power density, and energy storage density. The system operates at $T_{evaporator}$= 15 °C, $T_{sorption/condenser}$= 30 °C, and $T_{desorption}$= 90 °C, which are imposed by the application and ambient conditions. The system operating temperatures are used to calculate $\frac{p}{p_0}$, explained in Section 3.2, determining initial equilibrium concentration $''c_o''$ and final equilibrium concentration $''c_{eq}''$ which are needed for modeling the sorber bed, Eq. (12). Table 5 presents the baseline design parameters and their corresponding ranges considered in this study. The solution properties described in Table 4 are used for the analysis.

Fig. 6 shows specific cooling power (SCP) and cooling power density (CPD) plotted against various design parameters, including groove depth, groove top width, contact angle, groove wall thickness (for rectangular groove only), groove bottom width (for trapezoidal groove only), and cycle time. The following observations can be made.

i) Trapezoidal grooves exhibit higher SCP and CPD due to the reduced average film thickness resulting from an increased wall angle (β, see Fig. C1).
ii) Increasing the groove depth (Fig. 6a) decreases SCP for both trapezoidal and rectangular grooves, as the greater average film thickness introduces mass transfer resistance. However, CPD exhibits an optimum around a groove depth of 550 μm, considering sorbent mass and occupied volume factors. Consequently, a depth of 550 μm was chosen for microgroove fabrication in this study.
iii) Increasing the groove top width (Fig. 6b) results in higher SCP and CPD, as the average film thickness decreases.
iv) Increasing the contact angle (Fig. 6c) leads to a decrease in SCP and CPD due to the increased average film thickness.
v) For rectangular grooves (Fig. 6d), increasing the wall thickness enhances SCP by improving heat transfer from the sorbent to the heat exchanger. However, CPD decreases due to a reduction in sorbent mass.
vi) For trapezoidal grooves (Fig. 6e), increasing the groove bottom width causes a decrease in SCP due to the increased average film thickness. However, an optimum point exists for CPD considering sorbent mass and occupied volume factors.
vii) Decreasing the cycle time (Fig. 6f) results in higher SCP and CPD since the sorption rate is greater at the initial stage of the sorption process.

Among the parameters considered, cycle time and groove depth have the most significant impact on both SCP and CPD, while the contact angle has the least effect.

Fig. 7 shows energy storage density (ESD) at τ= 3 min and maximum energy storage density plotted against various design parameters, including groove depth, groove top width, contact angle, groove wall thickness (only for rectangular grooves), groove bottom width (only for trapezoidal grooves), and cycle time. It should be mentioned that ESD can be calculated at different cycle times. By increasing the time, the sorbent absorbs more water vapor until reaching the final equilibrium. ESD_{max} is calculated when the sorbent reaches its maximum capacity. However, we can also calculate ESD after a specific amount of time, which is not at the final equilibrium. The following observations can be made.

viii) Trapezoidal grooves generally provide a higher energy storage density at τ= 3 min, but a lower maximum energy storage density than rectangular grooves due to a lower sorbent mass.
ix) Increasing the groove depth (Fig. 7a) increases the maximum energy storage density for both grooves. The energy storage density at τ= 3 min has an optimum value, considering the kinetic aspect of the reaction.
x) Increasing the groove top width (Fig. 7b) increases the energy storage density at τ= 3 min for both grooves due to increased uptake. The maximum energy storage density has an optimum value for the rectangular grooves (maximum sorbent mass, balancing the effects of contact angle and wall thickness) and decreases with increasing groove top width for the trapezoidal grooves (due to increased wall thickness and thus decreased active mass).

Table 5
Baseline design parameters and their considered ranges.

Design parameters for rectangular channel	Baseline value	Range	Design parameters for trapezoidal channel	Baseline value	Range
Groove depth (μm)	600	400–800	Groove depth (μm)	600	400–800
Groove width (μm)	400	300–500	Groove top width (μm)	400	300–500
Wall thickness (μm)	60	20–120	Groove bottom width (μm)	300	200–400
Contact angle (deg)	20	0–40	Wall top thickness (μm)	20	–
Cycle time (min)	3	1–5	Contact angle (deg)	20	0–40
			Cycle time (min)	3	1–5

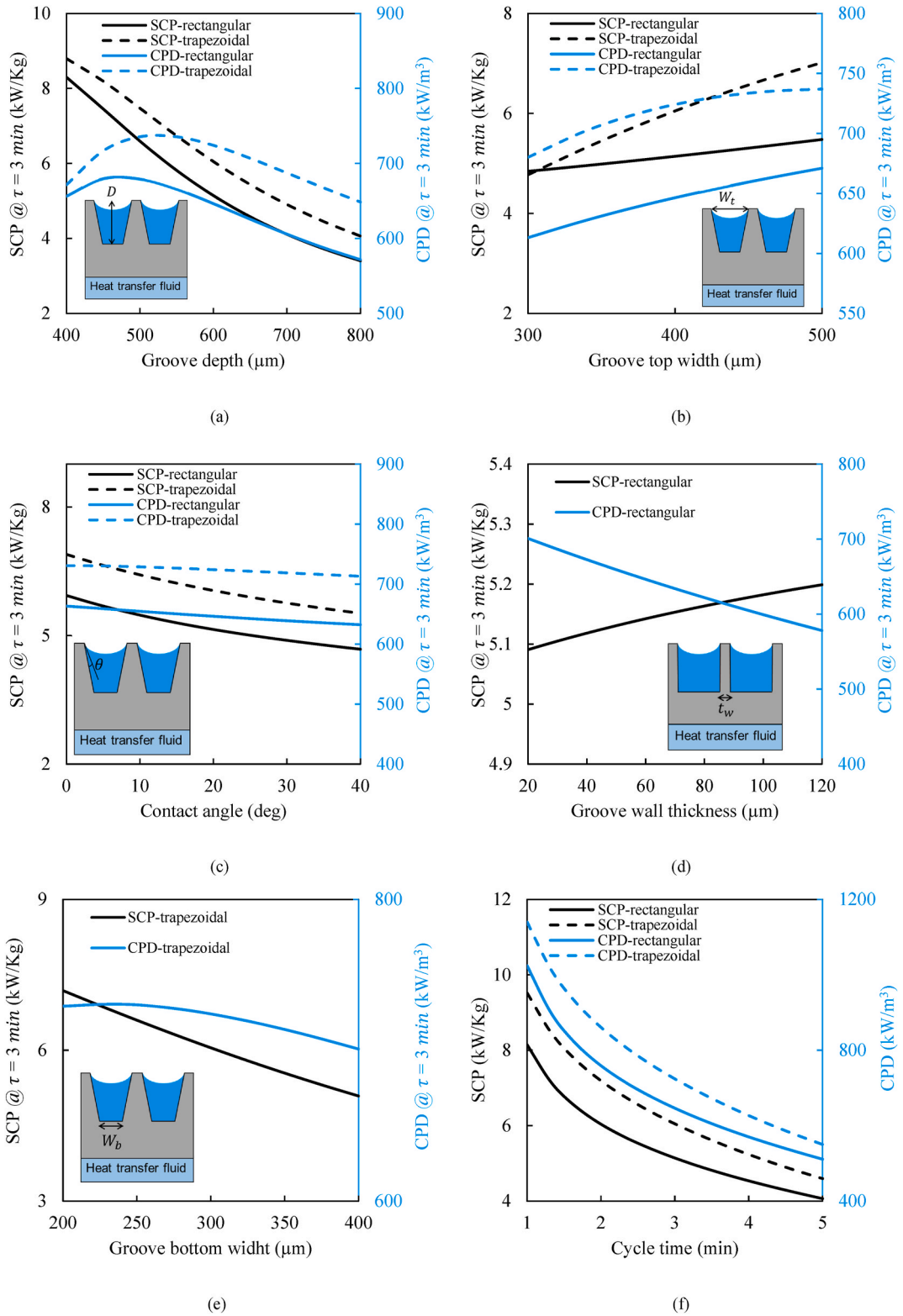

Fig. 6. Specific cooling power (SCP) and cooling power density (CPD) plotted against various design parameters: (a) groove depth, (b) groove top width, (c) contact angle, (d) groove wall thickness (for rectangular grooves only), (e) groove bottom width (for trapezoidal grooves only), and (f) cycle time.

xi) Increasing the contact angle (Fig. 7c) increases the maximum energy storage density for both grooves. However, the energy storage density at τ= 3 min decreases since the uptake is lower at a constant time with an increased contact angle.

xii) For the rectangular groove (Fig. 7d), both the energy storage density at τ= 3 min and the maximum energy storage density decrease with increasing wall thickness due to a reduction in sorbent mass.

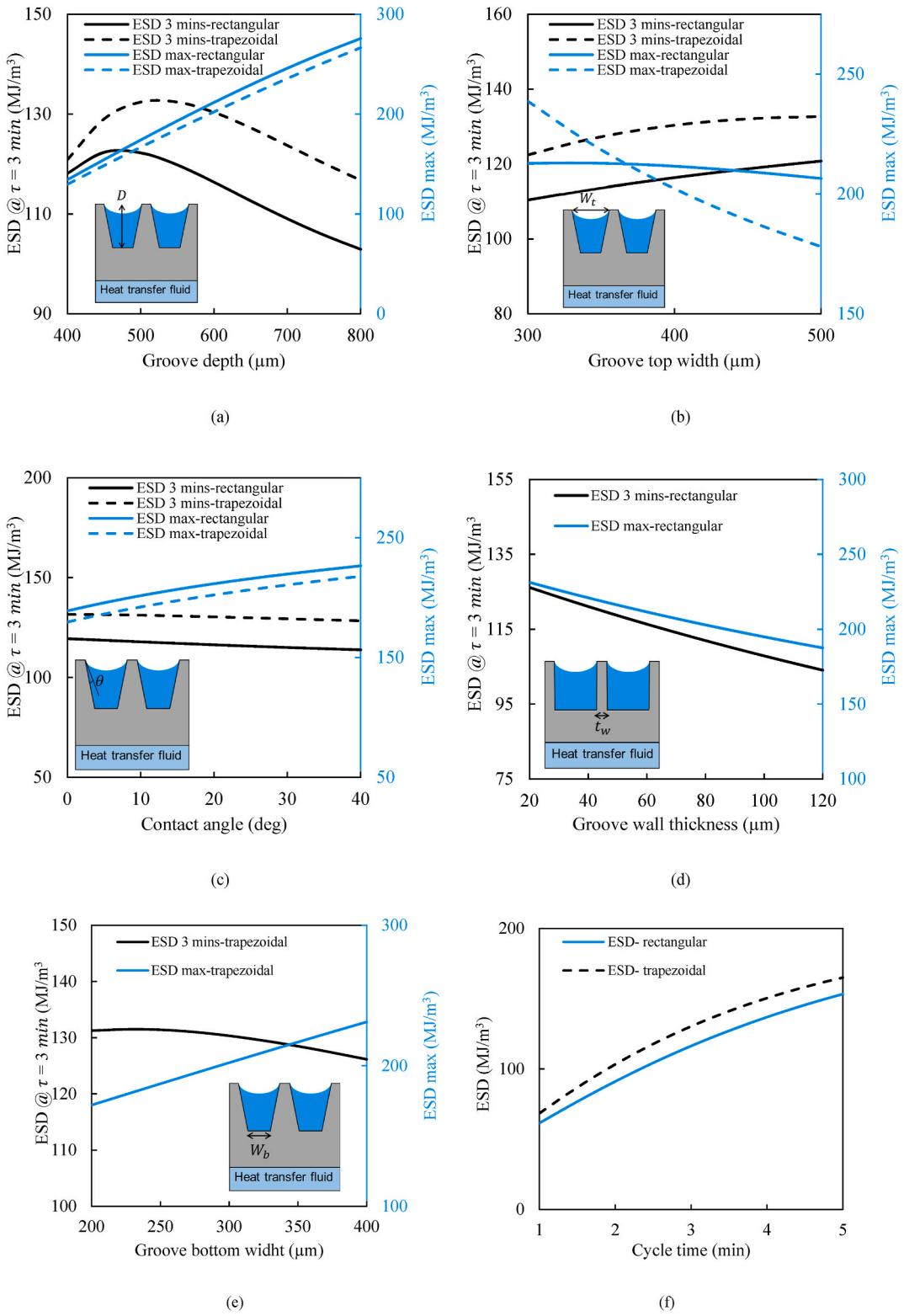

Fig. 7. Energy storage density at τ= 3 min and maximum energy storage density plotted against various design parameters: (a) groove depth, (b) groove top width, (c) contact angle, (d) groove wall thickness (for rectangular groove only), (e) groove bottom width (for trapezoidal groove only), and (f) cycle time.

xiii) For the trapezoidal groove (Fig. 7e), the maximum energy storage density increases with increasing groove bottom width due to an increase in sorbent mass. There is little variation in the energy storage density at τ= 3 min considering other factors as reduced uptake.

xiv) Increasing the cycle time (Fig. 7f) increases the energy storage density due to achieving higher uptake.

4.3. Comparison with available studies

Fig. 8 provides a comparison of the specific cooling power (SCP),

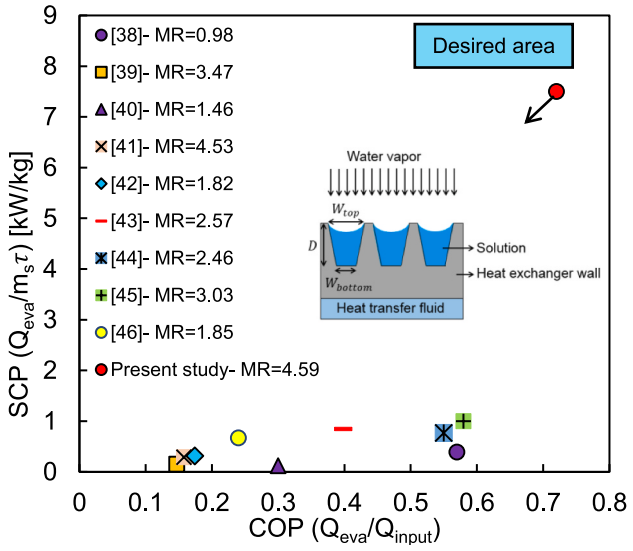

Fig. 8. Comparison of specific cooling power (SCP), coefficient of performance (COP), and mass ratio (MR) of the proposed microgroove-based absorber with relevant experimental studies [38–46].

coefficient of performance (COP), and mass ratio (MR) of the proposed microgroove-based absorber with recent experimental studies [38–46]. The comparison is based on experimental data collected under nominal operating conditions ($T_{evaporator}$= 15 °C, $T_{sorption/condenser}$= 30 °C, and $T_{desorption}$= 90 °C). The microgroove-based absorber exhibits superior performance in terms of SCP and COP at both material and system levels while maintaining a comparable MR to the existing studies.

The results demonstrate that the proposed microgroove-based absorber can achieve a specific cooling power of 7.6 kW/kg and a coefficient of performance of 0.71 with a cycle time of 3 min. The specific cooling power obtained by the microgroove-based absorber is up to seven times higher compared to similar systems studied in the literature.

Fig. 9 shows a comparison between the absorption rate of the present microgroove-based absorber, averaged over the sorption time, 90 s, and that of comparable experimental data for vertical, horizontal, and coil-type falling film absorbers [47–53]. The sorber bed temperature for all

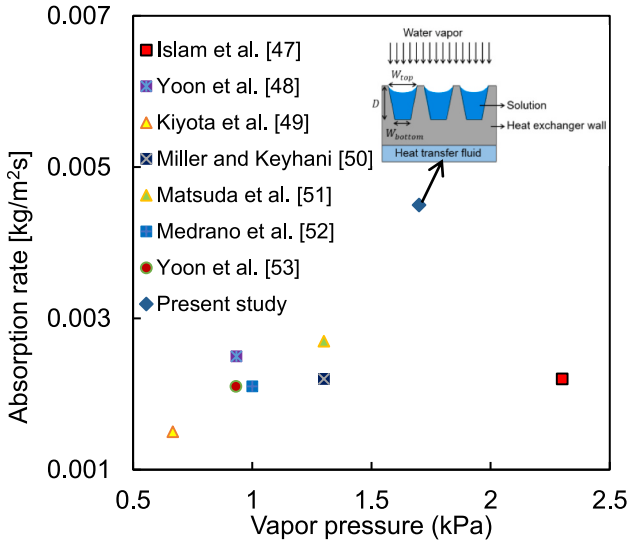

Fig. 9. Comparison between the absorption rate of the present microgroove-based absorber, averaged over sorption time, 90 s, and that of comparable experimental data for vertical, horizontal, and coil-type falling film absorbers [47–53].

the mentioned data is about 30 °C, but at different bed vapor pressures. As can be seen, the present sorber bed outperforms the experimental data in terms of absorption rate.

5. Conclusion

This study successfully modeled and experimentally validated a novel sorber bed design, namely the stationary thin film absorber, which can offer promising solutions for challenges encountered in oscillatory sorption heat transformation systems. Fabricating a microgrooved aluminum substrate and applying an oxide coating enabled the experimental evaluation of the proposed design. The analytical modeling of the coupled heat and mass transfer in the stationary thin film microgroove-based absorber provided a reliable framework for predicting its performance, further validated using experimental data.

Key design parameters were systematically investigated to understand their influence on specific cooling power, cooling power density, and energy storage density. Among the design parameters, cycle time and groove depth exhibited the most significant impact on specific cooling power and cooling power density, while the contact angle demonstrated the least influence. Also, trapezoidal grooves demonstrated higher specific cooling power and cooling power density, whereas the rectangular grooves offered a higher maximum energy storage density.

The present novel microgroove-based absorber achieved a specific cooling power of 7.6 kW/kg and a coefficient of performance of 0.71 with a cycle time of 3 min, demonstrating its superior performance compared to existing systems. The study highlighted the potential to achieve a specific cooling power up to seven times higher than comparable systems, emphasizing the advantages of the proposed microgroove-based absorber.

CRediT authorship contribution statement

Mahyar Ashouri: Writing – review & editing, Writing – original draft, Visualization, Validation, Software, Methodology, Investigation, Formal analysis, Data curation, Conceptualization. **Callum Chhokar:** Writing – review & editing, Writing – original draft, Visualization, Methodology, Investigation, Formal analysis, Data curation. **Majid Bahrami:** Writing – review & editing, Supervision, Project administration, Funding acquisition, Conceptualization.

Declaration of competing interest

The authors declare that they have no known competing financial interests or personal relationships that could have appeared to influence the work reported in this paper.

Data availability

Data will be made available on request.

Acknowledgements

This research is supported by funding from the Pacific Institute for Climate Solutions (PICS) Opportunity Grant (No. 36170-50280) and the Natural Sciences and Engineering Research Council of Canada (NSERC) Advancing Climate Change Science in Canada Grant (No. 536076-18). We acknowledge the support of the Natural Sciences and Engineering Research Council of Canada (NSERC) Collaborative Research and Training Experience program, CREATE (No. 554770-2021). This work made use of the 4D LABS shared facilities supported by the Canada Foundation for Innovation (CFI), British Columbia Knowledge Development Fund (BCKDF), Western Economic Diversification Canada (WD), and Simon Fraser University (SFU).

Appendix. A. Equation for the phase equilibrium of the LiBr-water solution

The following experimental correlations [33] can be used to calculate the equilibrium temperature and concentration for an LiBr-water solution [33]:

$$-\frac{1}{T}=a_1+a_2(1-c)+a_3\ln\left(\frac{1}{Pa}.p\right)+a_4(1-c)\ln\left(\frac{1}{Pa}.p\right)+a_5(1-c)^2+a_6\ln^2\left(\frac{1}{Pa}.p\right)+a_7(1-c)^2\ln\left(\frac{1}{Pa}.p\right)+a_8(1-c)\ln^2\left(\frac{1}{Pa}.p\right)$$
$$+a_9(1-c)^2\ln^2\left(\frac{1}{Pa}.p\right)+a_{10}(1-c)^3+a_{11}\ln^3\left(\frac{1}{Pa}.p\right)+a_{12}(1-c)^3\ln\left(\frac{1}{Pa}.p\right)+a_{13}(1-c)^3\ln^2\left(\frac{1}{Pa}.p\right)+a_{14}(1-c)\ln^3\left(\frac{1}{Pa}.p\right)$$
$$+a_{15}(1-c)^2\ln^3\left(\frac{1}{Pa}.p\right)+a_{16}(1-c)^3\ln^3\left(\frac{1}{Pa}.p\right) \tag{A.1}$$

where, T, c, and p, are the temperature, LiBr concentration, and pressure, respectively. Also, $a_{1\ to\ 16}$ are the corresponding constants, which are represented in Table A.1.

Table A.1
Constants for the phase equilibrium Eq. (A.1) [33].

Constant	Value	Constant	Value
a_1	-4.70858×10^{-3}	a_9	1.10477×10^{-4}
a_2	-1.276757×10^{-3}	a_{10}	4.915398×10^{-3}
a_3	1.45597×10^{-4}	a_{11}	-7.21234×10^{-8}
a_4	4.28261×10^{-4}	a_{12}	-5.8121×10^{-4}
a_5	9.48526×10^{-4}	a_{13}	-2.23738×10^{-5}
a_6	3.47501×10^{-6}	a_{14}	2.39788×10^{-6}
a_7	-4.95401×10^{-4}	a_{15}	-6.64049×10^{-6}
a_8	-5.44472×10^{-5}	a_{16}	4.26683×10^{-6}

Appendix. B. The Laplace transform method

To facilitate using the Laplace transform method, Meyer and Ziegler [33] applied first type boundary conditions for temperature and concentration at the vapor-solution interface, It is assumed that the mean temperature and concentration at the vapor-solution interface are unknown values but constant, as follows:

$$\overline{\theta}_{inf}=\frac{1}{Fo}\int_0^{Fo}\theta_{inf}d\widetilde{Fo} \tag{B.1}$$

$$\overline{\gamma}_{inf}=\frac{1}{Fo}\int_0^{Fo}\gamma_{inf}d\widetilde{Fo} \tag{B.2}$$

Equation (B.1) and (B.2) are used as the boundary conditions instead of Eq. (10). Then, the primary boundary conditions (Eq. (10)) are applied to the solution. By taking the Laplace transform with respect to variable "Fo", the following boundary conditions are achieved:

$$\Theta(s,0)=\frac{\theta_w}{s} \tag{B.3}$$

$$\frac{\partial\Upsilon(s,\eta=0)}{\partial\eta}=0 \tag{B.4}$$

$$\Theta(s,\eta=1)=\frac{\overline{\theta}_{inf}}{s} \tag{B.5}$$

$$\Upsilon(s,\eta=1)=\frac{\overline{\gamma}_{inf}}{s} \tag{B.6}$$

Similarly, by taking the Laplace transform from Eqs. (3) and (4), they are transformed into:

$$s.\Theta(s,\eta)=\frac{d^2\Theta(s,\eta)}{d\eta^2} \tag{B.7}$$

$$s.Le.\Upsilon(s,\eta)=\frac{d^2\Upsilon(s,\eta)}{d\eta^2} \tag{B.8}$$

By solving Eq. (B.7) and (B.8), temperature and concentration profiles in the Laplace space are as follows:

$$\Theta(s,\eta)=\frac{\overline{\theta}_{inf}}{s}\frac{\sinh(\sqrt{s}\,\eta)}{\sinh(\sqrt{s})}+\frac{\theta_w}{s}\frac{\sinh(\sqrt{s}\,(1-\eta))}{\sinh(\sqrt{s})} \tag{B.9}$$

$$\Upsilon(s,\eta)=\frac{\overline{\gamma}_{inf}}{s}\frac{\sinh\left(\sqrt{s.Le}\,\eta\right)}{\sinh\left(\sqrt{s.Le}\right)} \tag{B.10}$$

Temperature and concentration profiles in the LiBr-water solution are as follows:

$$\theta(Fo,\eta)=\left(\overline{\theta}_{inf}-\theta_w\right).\eta+\theta_w+\frac{2\overline{\theta}_{inf}}{\pi}\sum_{k=1}^{\infty}\frac{(-1)^k\,sin(k\pi\eta)}{k}e^{-k^2\pi^2Fo}+\frac{2\theta_w}{\pi}\sum_{k=1}^{\infty}\frac{(-1)^k\,sin(k\pi(1-\eta))}{k}e^{-k^2\pi^2Fo} \tag{B.11}$$

$$\gamma(Fo,\eta)=\overline{\gamma}_{inf}+\frac{4\overline{\gamma}_{inf}}{\pi}\sum_{k=0}^{\infty}\frac{(-1)^{k+1}\cos\left((2k+1)\frac{\pi}{2}\eta\right)}{2k+1}e^{-\frac{(2k+1)^2\pi^2}{4Le}Fo} \tag{B.12}$$

The boundary conditions at the vapor-solution interface should be satisfied to couple heat and mass transfer (see Eq. (10)). By taking the average of the boundary conditions at the vapor-solution interface with respect to the variable *"Fo"* and considering the definitions mentioned in Eq. (B.1) and (B.2), the following equations are obtained:

$$\frac{1}{Fo}\int_0^{Fo}\left(\theta_{inf}+\gamma_{inf}\right)d\widetilde{Fo}=\frac{1}{Fo}\int_0^{Fo}d\widetilde{Fo} \tag{B.13}$$

$$\frac{1}{Fo}\int_0^{Fo}\left.\frac{\partial\theta}{\partial\eta}\right|_{inf}d\widetilde{Fo}=\frac{\Lambda}{Le}\frac{1}{Fo}\int_0^{Fo}\left.\frac{\partial\gamma}{\partial\eta}\right|_{inf}d\widetilde{Fo} \tag{B.14}$$

By substituting Eq. (B.11) and (B.12) in Eq. (B.13) and (B.14), the mean temperature and concentration at the interface are obtained:

$$\overline{\gamma}_{inf}=\frac{\left(1+\frac{2\Phi}{Fo.\pi^2}\right)k_m(p_v-p_o)-k_mb_4\left(\frac{2\Psi}{Fo.\pi^2}+1\right)\theta_w}{k_mb_4\frac{8.\Omega.\Lambda}{Fo.\ \pi^2}+\left(\frac{8Leb_3}{Fo.\ \pi^2}\Omega+k_mb_5\right)\left(1+\frac{2\Phi}{Fo.\ \pi^2}\right)} \tag{B.15}$$

$$\overline{\theta}_{inf}=\frac{\left(1+\frac{2\Psi}{Fo.\pi^2}\right)\theta_w+\frac{8.\Omega.\Lambda}{Fo.\ \pi^2}\overline{\gamma}_{inf}}{1+\frac{2\Phi}{Fo.\pi^2}} \tag{B.16}$$

$$\Phi=\sum_{k=1}^{\infty}\frac{1}{k^2}\left(1-e^{-k^2\pi^2Fo}\right) \tag{B.17}$$

$$\Psi=\sum_{k=1}^{\infty}\frac{(-1)^k}{k^2}\left(1-e^{-k^2\pi^2Fo}\right) \tag{B.18}$$

$$\Omega=\sum_{k=0}^{\infty}\frac{1}{(2k+1)^2}\left(1-e^{-\frac{(2k+1)^2\pi^2}{4Le}Fo}\right) \tag{B.19}$$

To perform the calculations for the above-mentioned series, the first 15 terms are sufficient to obtain accurate results. Also, the average concentration of the solution, which is needed for the calculation of uptake, can be found as follows:

$$\overline{\gamma}(Fo)=\int_0^1\gamma(Fo,\eta)d\eta=\overline{\gamma}_{inf}+\frac{8\overline{\gamma}_{inf}}{\pi^2}\sum_{k=0}^{\infty}\frac{(-1)^{k+1}\sin\left((2k+1)\frac{\pi}{2}\right)}{(2k+1)^2}e^{-\frac{(2k+1)^2\pi^2}{4Le}Fo} \tag{B.20}$$

Appendix. C. Average film thickness and porosity

Average film thickness and porosity are calculated in this section. Considering trapezoidal grooves (Fig. C1), the following geometrical parameters can be obtained [54]:

$$R_m=\frac{D.tan(\beta)+0.5W_b}{cos(\beta+\theta)} \tag{C.1}$$

$$\vartheta=\arcsin\left(\frac{W_t}{2R_m}\right) \tag{C.2}$$

$$\beta=\arctan\left(\frac{W_t-W_b}{2D}\right) \tag{C.3}$$

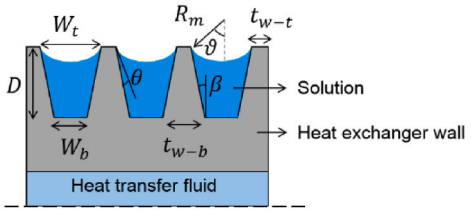

Fig. C1. Schematic of trapezoidal microgroove.

The cross-section area of the solution can be found as follows:

$$A_{cs}=\frac{W_t+W_b}{2}D+\frac{W_t}{2}\sqrt{R_m^2-\frac{W_t^2}{4}}-\vartheta R_m^2 \tag{C.4}$$

Therefore, the average film thickness is calculated as follows:

$$\delta_{ave}=\frac{A_{cs}}{W_t}=\frac{W_t+W_b}{2}\frac{D}{W_t}+0.5\sqrt{R_m^2-\frac{W_t^2}{4}}-\frac{\vartheta R_m^2}{W_t} \tag{C.5}$$

Also, the porosity used to calculate the equivalent thermal conductivity can be calculated as follows:

$$\phi=\frac{A_{cs}}{A_{cs}+A_w}=\frac{\frac{W_t+W_b}{2}D+\frac{W_t}{2}\sqrt{R_m^2-\frac{W_t^2}{4}}-\vartheta R_m^2}{D(t_{w-t}+W_t)} \tag{C.6}$$

Considering rectangular groove (Fig. C2), $W_t = W_b = W$ and β is equal to zero. The geometrical parameter can be calculated as follows [54]:

$$R_m=\frac{W}{cos(\theta)} \tag{C.7}$$

$$\vartheta=\arcsin\left(\frac{W}{2R_m}\right)$$

Accordingly, the average film thickness is calculated as follows:

$$\delta_{ave}=\frac{A_{cs}}{W}=D+0.5\sqrt{R_m^2-\frac{W^2}{4}}-\frac{\vartheta R_m^2}{W} \tag{C.8}$$

Also, the porosity used to calculate the equivalent thermal conductivity can be calculated as follows:

$$\phi=\frac{A_{cs}}{A_{cs}+A_{wall}}=\frac{D+0.5\sqrt{R_m^2-\frac{W^2}{4}}-\frac{\vartheta R_m^2}{W}}{D(t+W)} \tag{C.9}$$

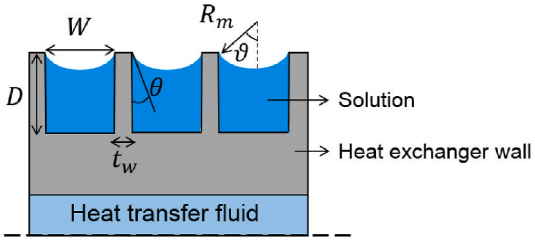

Fig. C2. Schematic of rectangular microgroove.

Appendix D. Contact angle measurements

Contact angle measurements were performed to assess the impact of the hybrid Al_2O_3/TiO_2 coating on surface wettability, as illustrated in Fig. D1. The reported values represent the average of five measurements. The experiments were conducted at a temperature of 21 °C and approximately 30 % relative humidity. A droplet volume of 3 μl was maintained for all measurements, while a 60 % concentration of aqueous LiBr was used.

The standard deviations for the uncoated and coated surfaces were approximately 4° and 3°, respectively. Notably, the contact angle observed on the coated substrate for aqueous LiBr (21°) exhibited a substantial reduction compared to that of the uncoated substrate for aqueous LiBr (81°). This result indicates a significant enhancement in surface wettability conferred by the hybrid Al_2O_3/TiO_2 coating.

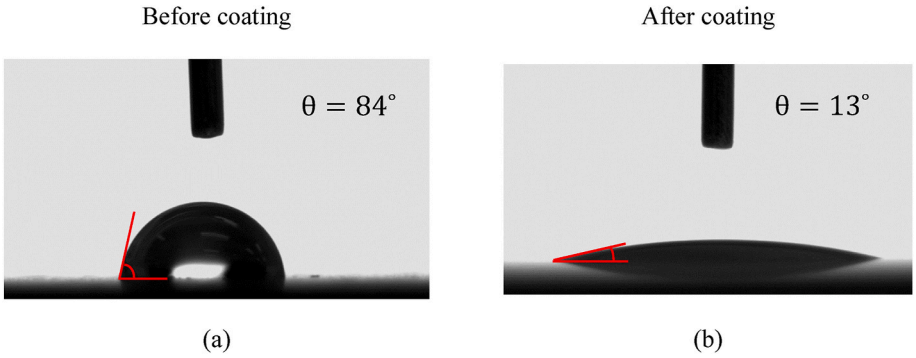

Fig. D1. Contact angles of aqueous LiBr on uncoated and coated surfaces. (a) Contact angle measurement of a 60 % LiBr droplet on the uncoated surface. (b) Contact angle measurement of a 60 % LiBr droplet on the coated surface. Measurements were performed five times at a temperature of 21 °C and approximately 30 % humidity, with a standard deviation of 3.5° (uncoated) and 2.8° (coated). The droplet volume used for the measurements was 3 μl.

References

[1] Huang P, Copertaro B, Zhang X, Shen J, Löfgren I, Rönnelid M, et al. A review of data centers as prosumers in district energy systems: renewable energy integration and waste heat reuse for district heating. Appl Energy 2020;258:114109.

[2] Xu ZY, Gao JT, Mao HC, Liu DS, Wang RZ. Double-section absorption heat pump for the deep recovery of low-grade waste heat. Energy Convers Manag 2020;220:113072.

[3] Hernández-Magallanes JA, Heard CL, Best R, Rivera W. Modeling of a new absorption heat pump-transformer used to produce heat and power simultaneously. Energy 2018;165:112–33.

[4] Yang S, Yang S, Wang Y, Qian Y. Low grade waste heat recovery with a novel cascade absorption heat transformer. Energy 2017;130:461–72.

[5] Ashouri M, Kheyrikoochaksarayee N, Chhokar C, Shabani A, Bahrami M. A big data-handling machine learning model for membrane-based absorber reactors in sorption heat transformers. Energy Convers Manag 2023;292:117376.

[6] Ashouri M, Elsafi AM, Girnik IS, Bahrami M. An analytical solution for heat and mass transfer in falling film absorption with arbitrary thermal boundary conditions. Appl Therm Eng 2023;231:120891. https://doi.org/10.1016/J.APPLTHERMALENG.2023.120891.

[7] Ding Z, Wu W, Huang S-M, Huang H, Bai Y, He Z. A novel compression-assisted energy storage heat transformer for low-grade renewable energy utilization. Energy 2023;263:125681.

[8] Huicochea A. A novel advanced absorption heat pump (Type III) for cooling and heating using low-grade waste heat. Energy 2023;278:127938.

[9] Ashouri M, Chhokar C, Bahrami M. Stationary thin film microgroove-based sorber reactor for sorption heat transformers: surface modification, sorption dynamics, and crystallization. Energy Convers Manag 2024;315:118780.

[10] Ashouri M, Bahrami M. Heat and mass transfer in laminar falling film absorption: a compact analytical model. Int J Heat Mass Transf 2022;188:122598. https://doi.org/10.1016/J.IJHEATMASSTRANSFER.2022.122598.

[11] Bahrehmand H, Bahrami M. Optimized sorber bed heat and mass exchangers for sorption cooling systems. Appl Therm Eng 2021;185:116348. https://doi.org/10.1016/j.applthermaleng.2020.116348.

[12] Rouhani M. Sorption thermal energy storage for sustainable heating and cooling. 2019.

[13] He F, Nagano K, Togawa J. Experimental study and development of a low-cost 1 kW adsorption chiller using composite adsorbent based on natural mesoporous material. Energy 2020;209:118365.

[14] Henninger SK, Ernst S-J, Gordeeva L, Bendix P, Fröhlich D, Grekova AD, et al. New materials for adsorption heat transformation and storage. Renew Energy 2017;110:59–68.

[15] Liu Z, Xu M, Huang C, Huai X. Performance evaluation of silicoaluminophosphate with SFO topology for water-sorption-driven heating and cooling systems. Appl Therm Eng 2022;216:119100.

[16] Barpaga D, Zheng J, McGrail BP, Motkuri RK. Manipulating pore topology and functionality to promote fluorocarbon-based adsorption cooling. Acc Chem Res 2021;55:649–59.

[17] Olajire AA. CO2 capture and separation technologies for end-of-pipe applications–A review. Energy 2010;35:2610–28.

[18] Zheng X, Ge TS, Wang RZ. Recent progress on desiccant materials for solid desiccant cooling systems. Energy 2014;74:280–94.

[19] Mehrabadi A, Farid M. New salt hydrate composite for low-grade thermal energy storage. Energy 2018;164:194–203.

[20] Freni A, Sapienza A, Glaznev IS, Aristov YI, Restuccia G. Experimental testing of a lab-scale adsorption chiller using a novel selective water sorbent "silica modified by calcium nitrate.". Int J Refrig 2012;35:518–24. https://doi.org/10.1016/J.IJREFRIG.2010.05.015.

[21] Nunez T, Henning H-M, Mittelbach W. High energy density heat storage system–achievements and future work. ISES Sol. Göteborg, Sweden: World Congr; 2003.

[22] Ashouri M, Bahrami M. On the absorption rate of membrane-based adiabatic sorber beds: an analytical approach. Int J Heat Mass Transf 2023;209:124105.

[23] Golparvar B, Niazmand H, Sharafian A, Ahmadian Hosseini A. Optimum fin spacing of finned tube adsorber bed heat exchangers in an exhaust gas-driven adsorption cooling system. Appl Energy 2018;232:504–16. https://doi.org/10.1016/J.APENERGY.2018.10.002.

[24] Tchernev DI. Exploration of molecular-sieve zeolites for the cooling of buildings with solar energy. Lincoln Lab; 1977. Final report 1 sep 74–31 Aug 75. Massachusetts Inst. of Tech., Lexington (USA).

[25] Ashouri M, Bahrami M. Analytical solution for coupled heat and mass transfer in membrane-based absorbers. Int J Heat Mass Transf 2022;192:122892.

[26] Castro J, Oliet C, Rodríguez I, Oliva A. Comparison of the performance of falling film and bubble absorbers for air-cooled absorption systems. Int J Therm Sci 2009;48:1355–66.

[27] Wu X, Xu S, Jiang M. Development of bubble absorption refrigeration technology: a review. Renew Sustain Energy Rev 2018;82:3468–82.

[28] Sehgal S, Alvarado JL, Hassan IG, Kadam ST. A comprehensive review of recent developments in falling-film, spray, bubble and microchannel absorbers for absorption systems. Renew Sustain Energy Rev 2021;142:110807.

[29] Bahrehmand H, Khajehpour M, Bahrami M. Finding optimal conductive additive content to enhance the performance of coated sorption beds: an experimental study. Appl Therm Eng 2018;143:308–15. https://doi.org/10.1016/J.APPLTHERMALENG.2018.07.115.

[30] Rouhani M, Bahrami M. Effective thermal conductivity of packed bed adsorbers: Part 2— Theoretical model. Int J Heat Mass Transf 2018;123:1212–20.

[31] Fumey B, Weber R, Baldini L. Heat transfer constraints and performance mapping of a closed liquid sorption heat storage process. Appl Energy 2023;335:120755.

[32] Faghri A. Heat pipe science and technology. Global Digital Press; 1995.

[33] Meyer T, Ziegler F. Analytical solution for combined heat and mass transfer in laminar falling film absorption using first type boundary conditions at the interface. Int J Heat Mass Transf 2014;73:141–51.

[34] Sharafian A, Mehr SMN, Huttema W, Bahrami M. Effects of different adsorber bed designs on in-situ water uptake rate measurements of AQSOA FAM-Z02 for vehicle air conditioning applications. Appl Therm Eng 2016;98:568–74.

[35] Gordeeva LG, Restuccia G, Freni A, Aristov YI. Water sorption on composites "LiBr in a porous carbon.". Fuel Process Technol 2002;79:225–31.

[36] Moffat RJ. Describing the uncertainties in experimental results. Exp Therm Fluid Sci 1988;1:3–17. https://doi.org/10.1016/0894-1777(88)90043-X.

[37] Giannetti N, Yamaguchi S, Saito K. Simplified expressions of the transfer coefficients on a partially wet absorber tube. Int J Refrig 2019;105:135–47. https://doi.org/10.1016/j.ijrefrig.2018.07.007.

[38] Sapienza A, Santamaria S, Frazzica A, Freni A. Influence of the management strategy and operating conditions on the performance of an adsorption chiller. Energy 2011;36:5532–8.

[39] Freni A, Russo F, Vasta S, Tokarev M, Aristov YI, Restuccia G. An advanced solid sorption chiller using SWS-1L. Appl Therm Eng 2007;27:2200–4.

[40] Sharafian A, Mehr SMN, Thimmaiah PC, Huttema W, Bahrami M. Effects of adsorbent mass and number of adsorber beds on the performance of a waste heat-driven adsorption cooling system for vehicle air conditioning applications. Energy 2016;112:481–93.

[41] Verde M, Corberan JM, de Boer R, Smeding S. Modelling of a waste heat driven silica gel/water adsorption cooling system comparison with experimental results. ISHPC Conf. Padua, Italy 2011:7–8.

[42] Aristov YI, Sapienza A, Ovoshchnikov DS, Freni A, Restuccia G. Reallocation of adsorption and desorption times for optimisation of cooling cycles. Int J Refrig 2012;35:525–31. https://doi.org/10.1016/J.IJREFRIG.2010.07.019.

[43] Wittstadt U, Füldner G, Laurenz E, Warlo A, Große A, Herrmann R, et al. A novel adsorption module with fiber heat exchangers: performance analysis based on driving temperature differences. Renew Energy 2017;110:154–61.

[44] Bahrehmand H, Bahrami M. An analytical design tool for sorber bed heat exchangers of sorption cooling systems. Int J Refrig 2019;100:368–79. https://doi.org/10.1016/J.IJREFRIG.2019.02.003.

[45] Bahrehmand H, Bahrami M. Optimized sorber bed heat and mass exchangers for sorption cooling systems. Appl Therm Eng 2021;185:116348. https://doi.org/10.1016/J.APPLTHERMALENG.2020.116348.
[46] Freni A, Bonaccorsi L, Calabrese L, Caprì A, Frazzica A, Sapienza A. SAPO-34 coated adsorbent heat exchanger for adsorption chillers. Appl Therm Eng 2015;82:1–7. https://doi.org/10.1016/J.APPLTHERMALENG.2015.02.052.
[47] Islam MR. Absorption process of a falling film on a tubular absorber: an experimental and numerical study. Appl Therm Eng 2008;28:1386–94.
[48] Yoon J-I, Phan TT, Moon C-G, Lee H-S, Jeong S-K. Heat and mass transfer characteristics of a horizontal tube falling film absorber with small diameter tubes. Heat Mass Transf 2008;44:437–44.
[49] Kiyota M, Morioka I, Matsuyama T. Steam absorption into aqueous lithium bromide solution films falling inside vertical pipes. Heat Transf Res Co-sponsored by Soc Chem Eng Japan Heat Transf Div ASME 2003;32:740–52.
[50] Miller WA, Keyhani M. The correlation of simultaneous heat and mass transfer experimental data for aqueous lithium bromide vertical falling film absorption. J Sol Energy Eng 2001;123:30–42.
[51] Matsuda A, Choi KH, Hada K, Kawamura T. Effect of pressure and concentration on performance of a vertical falling-film type of absorber and generator using lithium bromide aqueous solutions. Int J Refrig 1994;17:538–42.
[52] Medrano M, Bourouis M, Coronas A. Absorption of water vapour in the falling film of water–lithium bromide inside a vertical tube at air-cooling thermal conditions. Int J Therm Sci 2002;41:891–8.
[53] Yoon J-I, Kwon O-K, Bansal PK, Moon C-G, Lee H-S. Heat and mass transfer characteristics of a small helical absorber. Appl Therm Eng 2006;26:186–92.
[54] Ternet F, Louahlia-Gualous H, Le Masson S. Impact of microgroove shape on flat miniature heat pipe efficiency. Entropy 2018;20:44.